

Article

# Raman Diagnostics of Cathode Materials for Li-Ion Batteries Using Multi-Wavelength Excitation

Marcel Heber, Kathrin Hofmann and Christian Hess \* 

Eduard-Zintl-Institute for Inorganic and Physical Chemistry, Technical University of Darmstadt, Alarich-Weiss-Str. 8, 64287 Darmstadt, Germany; marcel.heber@web.de (M.H.); kathrin.hofmann@tu-darmstadt.de (K.H.)

\* Correspondence: christian.hess@tu-darmstadt.de; Tel.: +49-6151-16-21975; Fax: +49-6151-16-21979

**Abstract:** Lithium-ion batteries have been commonly employed as power sources in portable devices and are of great interest for large-scale energy storage. To further enhance the fundamental understanding of the electrode structure, we report on the use of multi-wavelength Raman spectroscopy for the detailed characterization of layered cathode materials for Li-ion batteries ( $\text{LiCoO}_2$ ,  $\text{LiNi}_x\text{Co}_{1-x}\text{O}_2$ ,  $\text{LiNi}_{1/3}\text{Mn}_{1/3}\text{Co}_{1/3}\text{O}_2$ ). Varying the laser excitation from the UV to the visible (257, 385, 515, 633 nm) reveals wavelength-dependent changes in the vibrational profile and overtone/combination bands, originating from resonance effects in  $\text{LiCoO}_2$ . In mixed oxides, the influence of resonance effects on the vibrational profile is preserved but mitigated by the presence of Ni and/or Mn, highlighting the influence of resonance Raman spectroscopy on electronic structure changes. The use of UV laser excitation (257, 385 nm) is shown to lead to a higher scattering efficiency towards Ni in  $\text{LiNi}_{1/3}\text{Mn}_{1/3}\text{Co}_{1/3}\text{O}_2$  compared to visible wavelengths, while deep UV excitation at 257 nm allows for the sensitive detection of surface species and/or precursor species reminiscent of the synthesis. Our results demonstrate the potential of multi-wavelength Raman spectroscopy for the detailed characterization of cathode materials for lithium-ion batteries, including phase/impurity identification and quantification, as well as electronic structure analysis.



**Citation:** Heber, M.; Hofmann, K.; Hess, C. Raman Diagnostics of Cathode Materials for Li-Ion Batteries Using Multi-Wavelength Excitation. *Batteries* **2022**, *8*, 10. <https://doi.org/10.3390/batteries8020010>

Academic Editors: Karim Zaghib and Yuesheng Wang

Received: 8 December 2021

Accepted: 24 January 2022

Published: 29 January 2022

**Publisher's Note:** MDPI stays neutral with regard to jurisdictional claims in published maps and institutional affiliations.



**Copyright:** © 2022 by the authors. Licensee MDPI, Basel, Switzerland. This article is an open access article distributed under the terms and conditions of the Creative Commons Attribution (CC BY) license (<https://creativecommons.org/licenses/by/4.0/>).

**Keywords:** lithium-ion batteries; cathode;  $\text{LiCoO}_2$ ; NMC; resonance Raman spectroscopy; multi-wavelength excitation; UV Raman spectroscopy

## 1. Introduction

Li-ion batteries already play a dominant role as power sources for portable devices. They are also of great importance regarding the development of larger scale devices used in more demanding applications, such as electric vehicles, allowing us to shift the power source in ground transportation from internal combustion engines to electrical propulsion [1]. Starting from  $\text{LiCoO}_2$ , alternative cathode materials have been developed, including olivine  $\text{LiFePO}_4$ , spinel  $\text{LiM}_2\text{O}_4$  (for instance,  $M = \text{Ni}$  and  $\text{Mn}$ ), layered oxides of  $\text{LiMO}_2$  (for instance,  $M = \text{Ni}$  and  $\text{Co}$ ,  $\text{Mn}$ ), and lithium-rich layered oxides  $x\text{Li}_2\text{MnO}_3(1-x)\text{LiMO}_2$  (for instance,  $M = \text{Ni}$  and  $\text{Co}$ ,  $\text{Mn}$ ) [2,3] An important aspect regarding optimization, concerns the (partial) replacement of cobalt by other 3d transition metals, i.e., nickel and/or manganese, due to availability and costs. While  $\text{LiNiO}_2$  shows a higher specific capacity than  $\text{LiCoO}_2$ , it possesses a low stability for storage; additionally, it is difficult to correctly adjust its stoichiometry. For example, Liu et al. reported a substantial capacity reduction from 215 mAh/g to 165 mAh/g after  $\text{LiNiO}_2$  storage for a month, while storage for a year resulted in a completely inactive material [4]. On the other hand, NMC oxides with the composition  $\text{LiNi}_{1/3}\text{Mn}_{1/3}\text{Co}_{1/3}\text{O}_2$  can achieve a reversible specific capacity of 200 mAh/g [5], whereas for lithium-rich oxides  $x\text{Li}_2\text{MnO}_3(1-x)\text{LiMO}_2$  (such as,  $M = \text{Ni}$ ,  $\text{Co}$  and  $\text{Mn}$ ), even higher capacities of over 250 mAh/g were demonstrated [6,7]. While mixtures of the three transition metals, Ni, Mn, and Co, are already used commercially, a detailed

understanding of their functioning and degradation will be important for developing the next generation of cathode materials [8,9].

Raman spectroscopy proved to be a powerful method for the characterization of electrode materials for lithium-ion batteries, providing important structural information, complementary to XRD, and enabling microscopy and in situ/operando measurements [10–18]. In addition, its application is straightforward, requiring no specific sample preparation. The scattering intensity of a solid material in normal Raman spectroscopy depends on a variety of factors, including the concentration and the Raman cross-section, and typically shows a weak dependence on the wavelength of the exciting laser. In contrast, in resonance Raman spectroscopy, which is based on the excitation of an electronic transition, a strong dependence on the laser wavelength is observed, providing access to enhanced Raman cross-sections and unique Raman signatures of different compounds or components within a material [19]. This may be of particular importance for the characterization of materials with a structural complexity, such as cathode materials for Li-ion batteries, which are known to exhibit complex vibrational signatures. In addition to sensitive phase identification, the resonance Raman spectra may be used for structural characterization under working conditions of the battery, as previously demonstrated for LiCoO<sub>2</sub>-based composite cathodes by using visible excitation wavelengths [20].

As a result of the variations in electronic structure, the exploitation of resonance enhancements for materials characterization requires, in principal, a wavelength tunable excitation laser to meet the resonance conditions for the electronic transitions of the material under study, but more frequently, lasers with fixed excitation wavelengths are employed. While Raman spectroscopy has been increasingly applied to cathode materials for Li-ion batteries [8,10,12,13], only few studies exploited the resonance Raman effects of layered cathode materials, i.e., LiCoO<sub>2</sub> [20,21], LiNiO<sub>2</sub> [21], LiMn<sub>2</sub>O<sub>4</sub> [22], LiNi<sub>0.8</sub>Co<sub>0.15</sub>Al<sub>0.05</sub>O<sub>2</sub> [23], LiNi<sub>x</sub>Mn<sub>2-x</sub>O<sub>4</sub> [24] and LiNi<sub>1/3</sub>Co<sub>1/3</sub>Mn<sub>1/3</sub>O<sub>2</sub> [25].

In this contribution, we present a multi-wavelength Raman spectroscopic study on layered cathode materials (LiCoO<sub>2</sub>, LiNi<sub>x</sub>Co<sub>1-x</sub>O<sub>2</sub>, LiNi<sub>1/3</sub>Mn<sub>1/3</sub>Co<sub>1/3</sub>O<sub>2</sub>) for Li-ion batteries. By using excitation ranging from the deep UV to the visible (257, 385, 515, 633 nm), we investigate for the first time the wavelength-dependent structural behavior of common cathode materials, thereby exploring the influence of resonance Raman effects on the spectral behavior. We discuss the potential of multi-wavelength spectroscopy, including UV Raman excitation for (electronic) structure analysis, quantification, phase and impurity identification, in battery materials.

## 2. Experimental Section

### 2.1. Preparation of Cathode Materials

For the preparation of the LiNi<sub>x</sub>Mn<sub>y</sub>Co<sub>z</sub>O<sub>2</sub> materials, we applied the Pechini process to ensure a statistical distribution of the cations [26]. Briefly, as precursors, LiNO<sub>3</sub> (Merck KGaA, ≥98%), Co(NO<sub>3</sub>)<sub>2</sub>·6H<sub>2</sub>O (Merck KGaA, ≥99.0%), Ni(NO<sub>3</sub>)<sub>2</sub>·6H<sub>2</sub>O (Puratronic, >99.99%), Mn(NO<sub>3</sub>)<sub>2</sub>·4H<sub>2</sub>O (Sigma Aldrich, 97%) and citric acid (AppliChem, ≥98%) were employed. After their dissolution in water, we added dropwise a concentrated ammonia solution (25%) until a pH value of 5 was reached. We then added ethylene glycol into the suspension and set the temperature to 180 °C for 6 h. As product, a black solid was obtained, which was first ground and then pre-calcined at 450 °C for 6 h (heating rate: 1.5 °C/min), yielding a brown powder, which was ground. LiCoO<sub>2</sub> was calcined at 800 °C for 20 h (heating rate: 20 °C/min), LiNi<sub>x</sub>Co<sub>1-x</sub>O<sub>2</sub> at 775 °C for 10 h (heating rate: 20 °C/min) and LiNi<sub>1/3</sub>Mn<sub>1/3</sub>Co<sub>1/3</sub>O<sub>2</sub> (NMC) at 900 °C for 15 h (heating rate: 20 °C/min). LiNiO<sub>2</sub> (Sigma-Aldrich, ≥98%) and other reference compounds were commercially available.

### 2.2. Characterization

*Raman Spectroscopy.* UV Raman spectra were recorded on a triple-stage spectrograph (Princeton Instruments, TriVista 555), equipped with a charge-coupled device (CCD, 2048 × 512 pixels) and by using 256.7 and 385.1 nm radiation generated by a Ti:sapphire

laser and frequency conversion crystals (Indigo Coherent). The spectral resolution of the spectrometer was approximately  $1\text{ cm}^{-1}$ . Great care was taken of the potential UV-induced effects, by using a UV Raman setup with a large spot size ( $0.6\text{ mm}^2$ ). The setup was based on a spherical mirror for laser excitation and parabolic mirrors for the collection of the scattered radiation. Based on this setup, we can avoid sample damage when using a low laser power of 3 mW. The analysis of the UV Raman data included cosmic ray removal and background subtraction. Prior to each measurement, the focus conditions were optimized using boron nitride (BN, 99%).

The Raman spectra at 514.5 nm excitation were recorded with an argon ion laser (Melles Griot), whereas for 632.8 nm spectra, a diode laser (Ondax) was employed as the light source. The Raman spectrometer (Kaiser Optical, HL5R) was equipped with an electronically cooled CCD detector ( $256 \times 1024$  pixels), and characterized by a spectral resolution of  $5\text{ cm}^{-1}$  and a wavelength stability of better than  $0.5\text{ cm}^{-1}$ . We adjusted the laser power to 0.8 mW as measured at the sample position. The Raman analysis included a cosmic ray removal and an auto new-dark correction. The acquisition time for a single spectrum was 600 s, including the application of a cosmic ray filter and subtraction of the dark spectrum (laser off).

In the following, the Raman excitation wavelengths 256.7, 385.1, 514.5, and 632.8 nm will be referred to as 257, 385, 515, and 633 nm, respectively.

*Diffuse Reflectance UV-Vis Spectroscopy.* For recording the diffuse reflectance (DR) UV-Vis spectra, we employed a UV-Vis spectrometer (Jasco V-770) and used D2 and halogen light sources. For analysis, a reaction cell (HVC-MRA-5, Harrick Scientific) was employed. MgO powder was used as a white standard in the same geometry as the sample.

*X-ray Diffraction.* For X-ray powder diffraction experiments, we employed an X-ray powder diffractometer (StadiP, Stoe & Cie GmbH) in transmission geometry, using Cu  $K_{\alpha 1}$  ( $\lambda = 1.540598\text{ \AA}$ ; Ge[111]-monochromator) radiation and a Mythen 1K (Dectris) detector, and Mo  $K_{\alpha 1}$  ( $\lambda = 0.70930\text{ \AA}$ ; Ge[111]-monochromator) radiation and a position-dependent (Stoe) detector. For analysis, the program WinXPOW (Stoe & Cie GmbH) and the program package GSAS-II was employed [27].

### 3. Results and Discussion

Prior analysis using multi-wavelength Raman spectroscopy allowed us to characterize the layered cathode materials ( $\text{LiCoO}_2$ ,  $\text{LiNi}_{0.2}\text{Co}_{0.8}\text{O}_2$ ,  $\text{LiNi}_{0.8}\text{Co}_{0.2}\text{O}_2$  and  $\text{LiNi}_{1/3}\text{Mn}_{1/3}\text{Co}_{1/3}\text{O}_2$ ) by using XRD. The XRD results confirm the phase purity and high crystallinity of the materials (see Supplementary Materials, Figures S1–S3).

#### 3.1. $\text{LiCoO}_2$

Figure 1 depicts the Raman spectra of  $\text{LiCoO}_2$  prepared by the Pechini process using 257, 385, 515, and 633 nm excitation. The two Raman active modes ( $E_g$ :  $486\text{ cm}^{-1}$ ;  $A_{1g}$ :  $595\text{ cm}^{-1}$ ) [28] are clearly visible in all spectra, but show variations in the intensity ratio with the excitation wavelength. The  $E_g$  mode involves mainly O–Co–O bending, and the  $A_{1g}$  mode Co–O stretching. As suggested by the corresponding UV-Vis spectrum (see Figure S4) and previously discussed by Gross et al., [20]. Raman spectra with an increased  $A_{1g}/E_g$  ratio are recorded under resonance conditions, thus leading to the appearance of overtone and combination bands. This is further supported by the Raman spectra obtained after the (partial) exchange of cobalt by nickel, as will be discussed below.  $\text{LiCoO}_2$  electronic transitions, which may be related to resonance Raman effects, are located at around 2.1 eV (591 nm), attributed to the d–d transition from  $\text{Co}_{t2g}$  to  $\text{Co}_{eg}$  bands, and above 3.3 eV (375 nm), originating from  $\text{Li}1s$  to  $\text{O}2p$  or  $\text{O}2p$  to  $\text{Co}3d$  transitions [29].

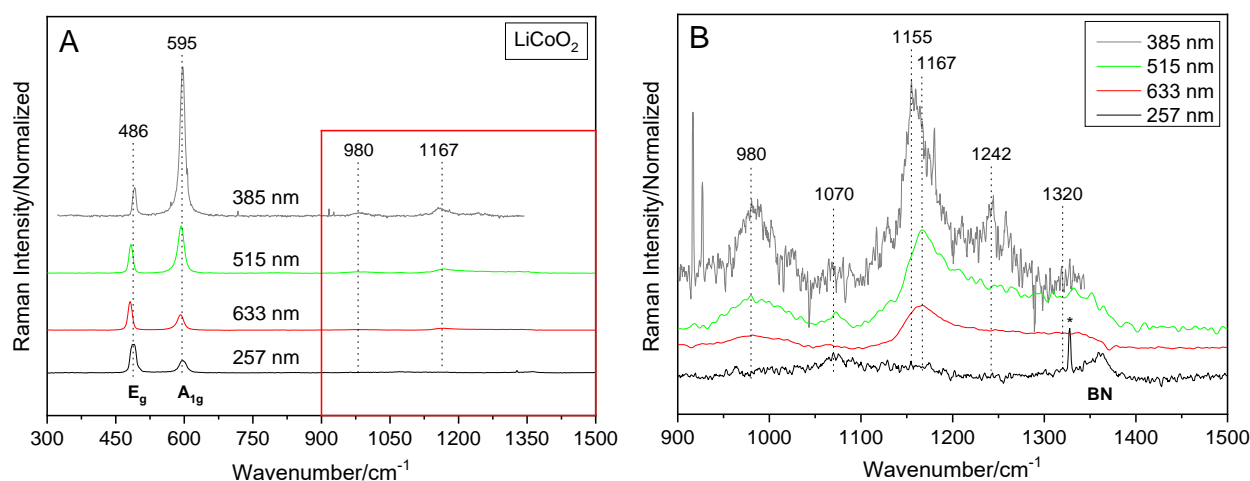


**Figure 1.** Raman spectra of  $\text{LiCoO}_2$  recorded with 257, 385, 515 and 633 nm laser excitations, normalized to the  $E_g$  signal and offset for clarity. (A) Survey spectra. (B) Detailed view of the overtone/combination band region (marked red in (A)). Note that the spectrum recorded at 257 nm excitation contains a cosmic ray spike (\*) and a signal from residual BN used for focus optimization.

Based on the Raman spectra in Figure 1, the  $A_{1g}/E_g$  intensity ratios were determined for all laser wavelengths by using the ratios of the peak heights. For the 633 and 515 nm excitations, the  $A_{1g}/E_g$  values of 0.5 and 1.65 were obtained, in agreement with our previous study [20]. A further decrease in the excitation wavelength to 385 nm leads to an increase in the intensity ratio to 5.3, while for deep UV excitation at 257 nm, a ratio drop to 0.4 is observed. Hence, the resonance enhancement of the  $A_{1g}$  band at  $\sim 595 \text{ cm}^{-1}$  is most pronounced at the 385 nm excitation, and leads to the appearance of a strong overtone signal at  $\sim 1170 \text{ cm}^{-1}$ . The right panel of Figure 1 gives an enlarged view of the overtone region. Interestingly, in addition to the  $A_{1g}$  overtone signal, additional smaller features are detected within  $950\text{--}1400 \text{ cm}^{-1}$ , i.e., at 980, 1070, 1167, 1242, 1320 and  $1360 \text{ cm}^{-1}$ . In the case of the 257 nm excitation, no overtone signals are detected, strongly suggesting the absence of resonance conditions. This is also supported by the lower absorption in the UV as compared to the visible region (see Figure S4). Accordingly, the Raman band observed at around  $1070 \text{ cm}^{-1}$  for 257 nm excitation is attributed to a surface species (see discussion below), whereas the feature at  $1360 \text{ cm}^{-1}$  originates from residual BN used for focus optimization.

In the following, we will address the origin of the Raman features in the  $950\text{--}1400 \text{ cm}^{-1}$  region. First, it is noteworthy that there is an enhancement of the signals at 980 and  $\sim 1160 \text{ cm}^{-1}$ , which increases with the decreasing wavelength of the excitation laser, i.e.,  $633 \text{ nm} < 515 \text{ nm} < 385 \text{ nm}$ . The appearance of overtones at 633 nm excitation, despite the lower  $A_{1g}/E_g$  ratio, suggests the presence of a pre-resonance. The application of group theory to  $\text{LiCoO}_2$  (point group  $D_{3d}$ ) facilitates the assignment of the observed Raman features (see Table S1). In addition to the fundamental  $E_g$  and  $A_{1g}$  modes, the band assignments include overtones of the fundamental Raman active phonon modes ( $A_{1g}$ ,  $E_g$ ), the IR active modes ( $A_{2u}$ ,  $E_u$ ) and combination bands ( $A_{1g} \times E_g$ ,  $A_{2u} \times E_u$ ). Accordingly, the signal at  $980 \text{ cm}^{-1}$  is attributed to the overtone of the  $E_g$  mode of  $\text{LiCoO}_2$ , while the weak feature at  $1070 \text{ cm}^{-1}$  detected for 385, 515 and 633 nm excitations under (pre)-resonance conditions can be assigned to a combination band of the  $A_{1g}$  and  $E_g$  modes, with a possible contribution from an  $E_u$  overtone. According to Rao et al. [30] and Julien [31], the IR spectrum of  $\text{LiCoO}_2$  is characterized by an intense signal at  $595 \text{ cm}^{-1}$  with a shoulder towards higher wavenumbers, which are assigned to the  $\nu(\text{MO}_6)$ -mode of a  $\text{CoO}_6$  unit ( $A_{2u}$ ). It was postulated that the signal at  $595 \text{ cm}^{-1}$  originates from the cobalt ions occupying its regular site and the shoulder at  $653 \text{ cm}^{-1}$  from cobalt ions in an octahedral void in the lithium layer; the signal at  $526 \text{ cm}^{-1}$  was attributed to a  $\delta(\text{O-C-O})$ -mode ( $E_u$ ). Based on these assignments, the signal at  $1167 \text{ cm}^{-1}$  (see Figure 1B) may draw

a contribution from the  $A_{2u}$  overtone, in addition to the overtone of the  $A_{1g}$  phonon. The position of the broad Raman band at  $\sim 1320\text{ cm}^{-1}$  is consistent with the overtone of the IR active  $A_{2u}$  mode. This shows that the defect structure of cobalt ions in  $\text{LiCoO}_2$  may become accessible under resonance conditions. The feature at  $1155\text{ cm}^{-1}$  is located very close to that at  $1167\text{ cm}^{-1}$ , and may draw a contribution from a combination band of the  $A_{2u}$  and  $E_u$  modes. Finally, the Raman signal at  $1242\text{ cm}^{-1}$ , only observed for excitation at  $385\text{ nm}$  (see Figure 1B), may result from the overtone of the inactive fundamental  $A_{2u}$  mode. The assignments of the observed Raman features for  $\text{LiCoO}_2$  are summarized in Table 1.

**Table 1.** Assignment of the observed Raman bands for  $\text{LiCoO}_2$ .

Fundamental ( $\text{cm}^{-1}$ )	Overtone/Combination ( $\text{cm}^{-1}$ )	Assignment
486	980	$E_g$ $2E_g$
	1070	$2E_u, A_{1g} \times E_g$
595	1155, 1167	$A_{1g}$ $A_{2u} \times E_u, 2A_{1g}, 2A_{2u}$
	1242	$2A_{2u}$
	1320	$2A_{2u}$

### 3.2. $\text{LiNi}_y\text{Co}_{1-y}\text{O}_2$

Figure 2 depicts the Raman spectra of the fundamental (left panel) and overtone/combination (right panel) band region of  $\text{LiCoO}_2$  and  $\text{LiNi}_x\text{Co}_{1-x}\text{O}_2$  recorded at  $515\text{ nm}$  (A, B) and  $257\text{ nm}$  (C, D) excitations. As can be seen in the left panels, the  $A_{1g}$  and  $E_g$  Raman signals show a strong decrease in the intensity and a red-shift with an increasing amount of nickel, whereas the red-shift is more pronounced for the  $A_{1g}$  mode. At first sight, a similar behavior is observed for visible and UV excitation, as well as for the other excitation wavelengths (not shown). The presence of the two Raman bands ( $A_{1g}, E_g$ ) for  $\text{LiNi}_{0.2}\text{Co}_{0.8}\text{O}_2$  is consistent with the formation of mixed nickel–cobalt layers, i.e., a solid solution isomorphous with the pure phases. The observed red-shift can be explained by the expansion of the unit cell upon nickel substitution [10]. The increasing Ni content leads to a broadening of the Raman bands, especially the  $E_g$  mode, which is attributed to cation mixing in the crystal layers of the Ni-rich compounds [21]. The broadening of the phonon modes in  $\text{LiNi}_{0.8}\text{Co}_{0.2}\text{O}_2$  makes a more detailed (quantitative) analysis challenging. Interestingly, in case of  $257\text{ nm}$  excitation, an additional Raman feature is detected at around  $530\text{ cm}^{-1}$ . Upon closer inspection, such a contribution may also be identified in the visible spectra of  $\text{LiNi}_{1-x}\text{Co}_x\text{O}_2$  compounds in this work (see Figure 2A), as well as in the literature spectra [31]. To the best of our knowledge, the origin of this feature has not been addressed yet. For the  $257\text{ nm}$  excitation, the Raman spectrum of bare  $\text{LiNiO}_2$  exhibits a broad feature with a maximum at  $\sim 520\text{--}530\text{ cm}^{-1}$  (see Figure 5). Hence, the  $530\text{ cm}^{-1}$  Raman feature observed for  $\text{LiNi}_{0.8}\text{Co}_{0.2}\text{O}_2$  may indicate the presence of  $\text{LiNiO}_2$  domains. However, as UV excitation leads to highest surface sensitivity among the excitation wavelengths used in this study (see also below), we cannot exclude a contribution from surface phonons.

Upon substitution of cobalt by nickel, the Raman intensity of the fundamental modes decreases dramatically, independent of the excitation wavelength, as depicted in Figure S5 for the  $A_{1g}$  mode. Furthermore, as can be seen in Figure 2B, the overtone/combination bands strongly decline and have completely disappeared for  $\text{LiNi}_{0.8}\text{Co}_{0.2}\text{O}_2$ . On the other hand, with the increasing nickel content, we do not detect any new overtone features. Please note that the features detected in the overtone region for the  $257\text{ nm}$  excitation (see Figure 2D) can be fully accounted for by cosmic ray spikes, surface signals as well as residual BN used for focus optimization in the UV.

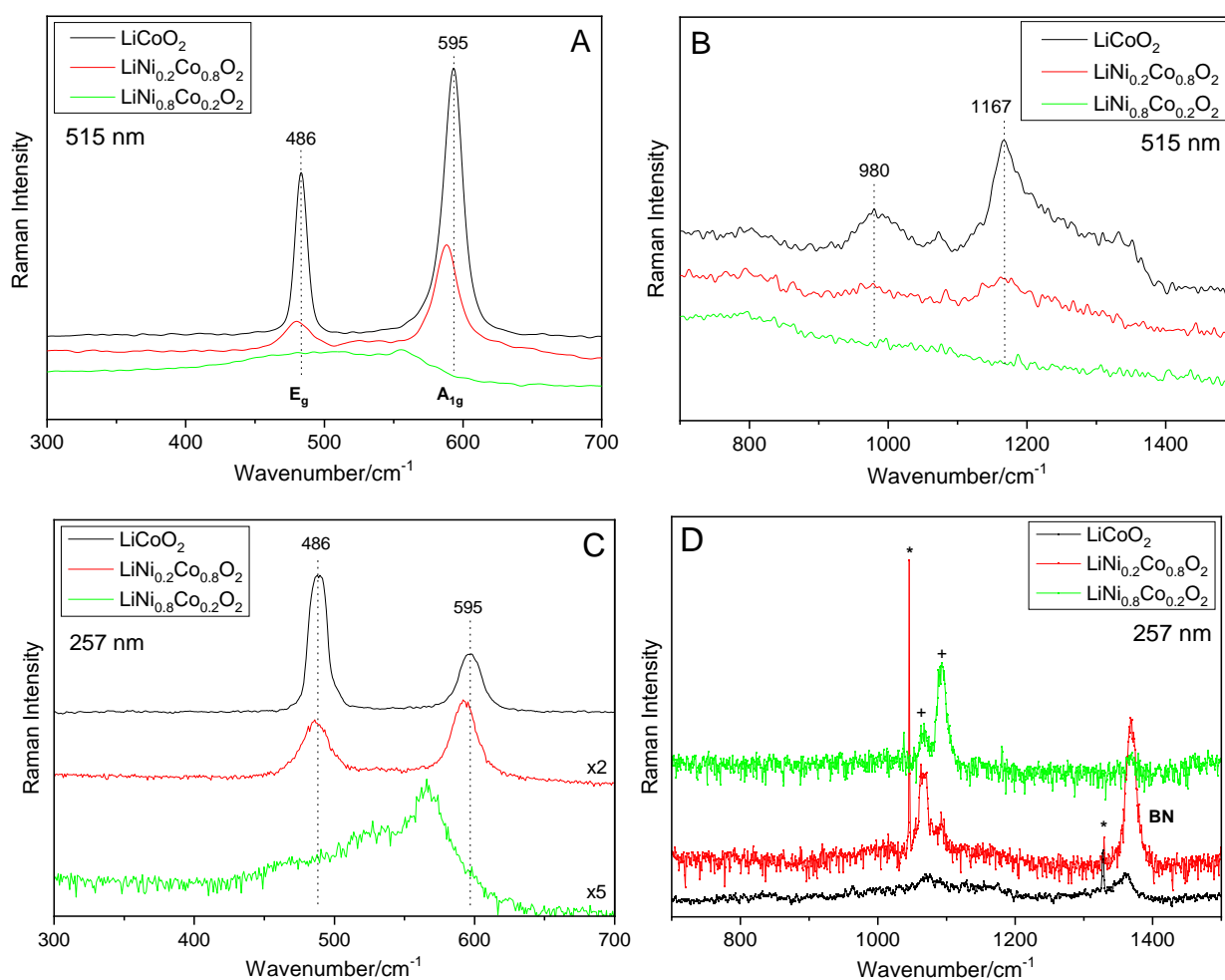


**Figure 2.** Raman spectra of  $\text{LiCoO}_2$  and  $\text{LiNi}_y\text{Co}_{1-y}\text{O}_2$  recorded at 515 nm (A,B) and 257 nm (C,D) laser excitations, showing the fundamental modes (left) and the overtone/combination band region (right). Spectra are offset for clarity. Note that the spectrum recorded at 257 nm excitation contains cosmic ray spikes (\*), surface signals (+) and a signal from residual BN used for focus optimization.

The observed intensity changes in the fundamental and overtone region of the Raman spectra clearly show the influence of nickel on the electronic structure of the mixed lithium nickel–cobalt oxides. Previously, in the context of lithium deintercalation from  $\text{LiCoO}_2$ , the strong decrease in Raman intensity has been associated with a reduction of the rhombohedral distortion by increasing the Ni content [31] and/or a skin depth effect [32]. To this end, the literature results suggested a higher electrical conductivity of  $\text{LiNiO}_2$  compared to  $\text{LiCoO}_2$  [33–35]. From this behavior of the bare oxides, we may expect an increased electrical conductivity, which decreases the optical skin depth of the excitation laser, thus resulting in a reduced scattering efficiency for the higher nickel content in  $\text{LiNi}_{1-x}\text{Co}_x\text{O}_2$  [32]. As can be seen in Figure 2 and Figure S5, such a scenario is fully consistent with our Raman results. Note that the Raman spectra show a broadening of the  $E_g$  mode with an increasing nickel content, which is associated with the non-stoichiometry induced by the presence of extra nickel [36].

The disappearance of the overtone/combination features in Figure 2B demonstrates that the presence of nickel significantly changes the conditions for resonance Raman spectroscopy, and thus the electronic structure in  $\text{LiNi}_{1-x}\text{Co}_x\text{O}_2$ . The substitution of cobalt by nickel leads to a gradual disappearance of the overtone/combination bands, but at the same time, we do not detect any new features in the overtone region for any of the excitation wavelengths (257, 385, 515, 633 nm), indicative of the presence of new resonance

effects. While our results highlight the sensitivity of resonance Raman spectroscopy for the electronic structure changes in  $\text{LiNi}_{1-x}\text{Co}_x\text{O}_2$ , a more detailed description would require the input from theoretical calculations.

Figure 3 depicts the observed red-shift in  $A_{1g}$  position with an increasing amount of nickel in  $\text{LiNi}_x\text{Co}_{1-x}\text{O}_2$  for 257 nm (A) and 515 nm (B) laser excitations. We observe a linear dependence of the  $A_{1g}$  position on the nickel content for all the excitation wavelengths, which give spectra of an acceptable quality, i.e., 257, 517 and 633 nm. From a linear fit to the data, the slopes of  $-39.8 \pm 3.7 \text{ cm}^{-1}/x$  (257 nm),  $-47.3 \pm 2.8 \text{ cm}^{-1}/x$  (515 nm) and  $-47.8 \pm 2.0 \text{ cm}^{-1}/x$  (633 nm) were obtained, where  $x$  represents the nickel content. Thus, within the error of the experiment, we find the red-shift of the  $A_{1g}$  mode to be independent of the excitation wavelength. The right panel also contains literature data from Julien recorded at 515 nm excitation for comparison [29]. While the dependence of the  $A_{1g}$  position on the nickel content shows the same tendency, a deviation from the linear behavior was observed, which may be associated with the cation disorder in the mixed oxide, resulting from the extensive calcination of 15 h at 750 °C (twofold), in contrast to the 10 h calcination at 775 °C applied in this work.

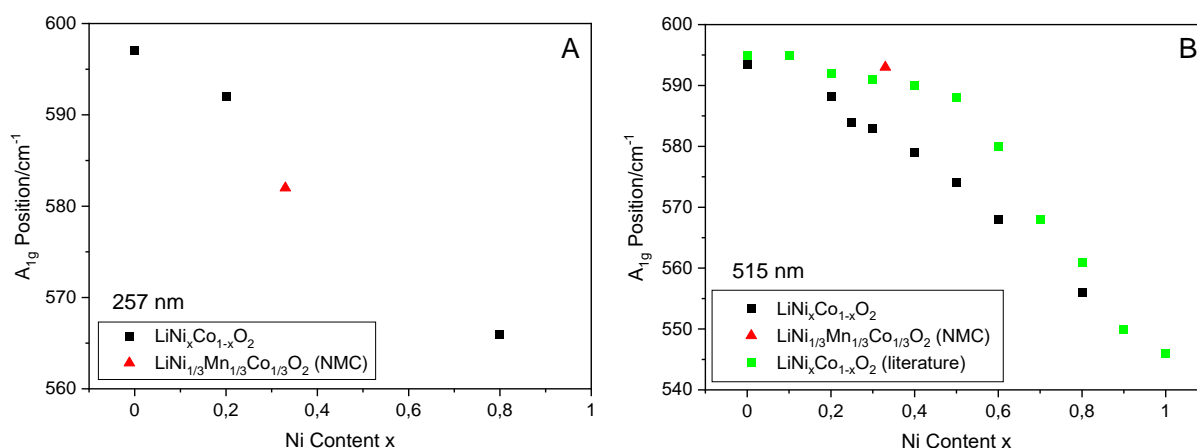


**Figure 3.** Position of the  $A_{1g}$  Raman mode for  $\text{LiNi}_x\text{Co}_{1-x}\text{O}_2$  as a function of the Ni content  $x$  for 257 nm (A) and 515 nm (B) laser excitations. For comparison, our data for  $\text{LiNi}_{1/3}\text{Mn}_{1/3}\text{Co}_{1/3}\text{O}_2$  (red) as well as 515 nm literature data [29] for  $\text{LiNi}_x\text{Co}_{1-x}\text{O}_2$  (green) was added.

For comparison, Figure 3 contains data for  $\text{LiNi}_{1/3}\text{Mn}_{1/3}\text{Co}_{1/3}\text{O}_2$  (NMC), which suggests that the nickel content may be determined quantitatively at 257 nm excitation, while the use of 515 nm excitation leads to significant deviations from the linear behavior. Accordingly, the  $A_{1g}$  intensity of NMC is consistent with the exponential decay curve obtained for  $\text{LiNi}_y\text{Co}_{1-y}\text{O}_2$  at 257 nm excitation, in contrast to the 515 nm behavior. Compared to the mixed lithium nickel cobalt oxides, the NMC material was calcined under harsher conditions, i.e., 15 h at 900 °C. It thus appears that a 515 nm laser excitation is more sensitive to the detailed state of the material. A discussion of the Raman analysis of NMC, including the role of manganese, will be presented in the next section.

To summarize, the above results demonstrate the potential of Raman spectroscopy for the quantification of the nickel content in  $\text{LiNi}_x\text{Co}_{1-x}\text{O}_2$  materials. The results suggest that if an appropriate excitation wavelength is chosen, NMC materials and possibly also other nickel containing layered materials can be analyzed. This is a very promising perspective, considering the importance of nickel in the development of novel cathode materials.

### 3.3. $\text{LiNi}_{1/3}\text{Mn}_{1/3}\text{Co}_{1/3}\text{O}_2$ (NMC)

The Raman spectra of NMC are characterized by a strong dependence on the excitation wavelength. As shown in Figure 4, pronounced differences in the Raman spectra are observed for the 257, 385 and 515/633 nm excitations. NMC has been proposed to represent a  $\text{LiMO}_2$  mixed oxide derived from the compounds  $\text{LiCoO}_2$ ,  $\text{LiNiO}_2$  and  $\text{LiMnO}_2$

( $M = \text{Ni} + \text{Co} + \text{Mn}$ ). Considering the first coordination shell only, the Raman spectra of NMC may be expected to consist of a combination of six signals, with each of the three oxides,  $\text{LiCoO}_2$ ,  $\text{LiNiO}_2$  and  $\text{LiMnO}_2$ , contributing an  $E_g$  and  $A_{1g}$  mode [37–39]. However, as can be seen from Figure 4, due to the complexity of the recorded Raman spectra, an unambiguous fit analysis aiming at a quantitative description is not feasible. This is in agreement with the results of previous studies, showing the challenge of Raman band assignments in NMC mixed oxides [12]. In this context, it has been pointed out that the NMC Raman profile represents more than the individual contributions ( $\text{LiCoO}_2$ ,  $\text{LiNiO}_2$ ,  $\text{LiMnO}_2$ ) summed up according to their proportion, and, in particular, the presence of multiple interactions between metal ions changing their local environments, but also the sample preparation, the experimental conditions as well as Raman spectroscopic aspects. In the following, we will therefore discuss the wavelength-dependent behavior of the NMC Raman spectra on a qualitative basis, which still provides a valuable insight into structural properties.

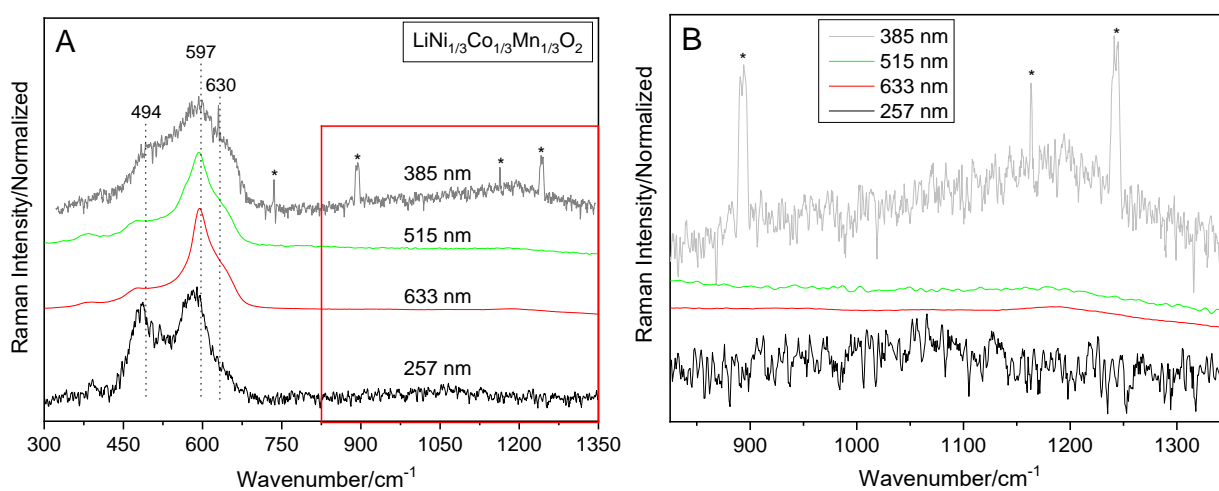


**Figure 4.** Raman spectra of  $\text{LiNi}_{1/3}\text{Mn}_{1/3}\text{Co}_{1/3}\text{O}_2$  (NMC) recorded with 257, 385, 515 and 633 nm laser excitations, normalized to the  $A_{1g}$  signal and offset for clarity. (A) Survey spectra. (B) Detailed view of the overtone/combination band region (marked red in (A)). Spectra recorded at 257 and 385 nm excitations contain cosmic ray spikes (\*).

Apparently, the Raman spectra of NMC are more complex than those of  $\text{LiCoO}_2$ . However, an indication for the presence of Co in NMC is readily provided by the overtone/combination band region measured by the 385 nm excitation (see Figure 4B), which shows a Raman signal at  $1190\text{ cm}^{-1}$ . As expected, this signal is significantly weaker than that observed for  $\text{LiCoO}_2$  (see Figure 1B). Nevertheless, its detection at 385 nm excitation strongly suggests the presence of resonance Raman effects operating in a similar manner, as in the case of  $\text{LiCoO}_2$ . Consistent with the wavelength-dependent behavior observed for  $\text{LiCoO}_2$ , an overtone feature is also observed for the 515 and 633 nm excitations, in contrast to the deep UV Raman spectrum (see Figure 4B).

The Raman spectra of NMC are characterized by major contributions located at around  $494$ ,  $597$  and  $630\text{ cm}^{-1}$ . While these contributions can be clearly observed for all excitation wavelengths, different intensity ratios are detected for 257, 385 and 515/633 nm excitations. Upon closer inspection, additional Raman features can be identified as a separate band at around  $380\text{ cm}^{-1}$  (257, 515, 633 nm) and as a shoulder at around  $560\text{ cm}^{-1}$  (515 nm). Although not directly detectable (as a band or shoulder), the latter feature may also contribute to the 257 and 385 nm spectra. In addition to the Co-related  $E_g$  and  $A_{1g}$  features ( $\sim 494\text{ cm}^{-1}$ ,  $\sim 597\text{ cm}^{-1}$ ), previous Raman studies on NMC materials have associated features at around  $470\text{ cm}^{-1}$  with the presence of Ni, features at around  $530\text{ cm}^{-1}$  with the presence of Ni (and Mn) and features  $> 600\text{ cm}^{-1}$  with the presence of Mn [25,37–39]. A smaller contribution

(shoulder)  $< 425\text{ cm}^{-1}$  was previously observed for NMC, but also for  $\text{LiNi}_{0.8}\text{Co}_{0.15}\text{Al}_{0.05}\text{O}_2$  (NCA) materials [12,25,39], thus showing no ion specificity.

Turning to the wavelength-dependent spectral behavior, most noticeable are the different vibrational profiles in the fundamental region in addition to the overtone properties discussed above. Considering the intensity ratios detected for  $\text{LiCoO}_2$  (see Figure 1A), we can first of all conclude that the presence of Ni and Mn has a pronounced effect on all spectral profiles. Interestingly, there are major differences in the intensity ratio of the NMC features around  $494$  and  $597\text{ cm}^{-1}$  for visible ( $515$ ,  $633\text{ nm}$ ), near UV ( $385\text{ nm}$ ) and deep UV ( $257\text{ nm}$ ) excitations. Compared to  $\text{LiCoO}_2$ , for the visible excitation, the  $494\text{ cm}^{-1}/597\text{ cm}^{-1}$  intensity ratio (I) is strongly reduced, whereas for near UV excitation a slight and for deep UV excitation a strong increase in I is observed. Furthermore, in case of UV excitation, the spectral profile contains additional scattering intensity at around  $530\text{ cm}^{-1}$ . These differences are more pronounced than those detected for the shoulder at around  $630\text{ cm}^{-1}$ , which is slightly reduced in intensity for  $257\text{ nm}$  excitation, compared to the laser wavelengths. Hence, we can state that UV excitation emphasizes the Raman scattering in NMC within  $450\text{--}550\text{ cm}^{-1}$ . Based on the previous literature assignments discussed above, phonons in this region may be associated with the presence of Ni and/or Mn. However, due the absence of major wavelength-dependent differences of the shoulder feature at round  $600\text{ cm}^{-1}$  (and considering its univocal association with Mn), the observed intensity increase can be related to the presence of Ni. We therefore conclude that the use of UV laser excitation ( $257$ ,  $385\text{ nm}$ ) leads to a higher scattering efficiency towards Ni in NMC, compared to the visible wavelengths ( $515$ ,  $633\text{ nm}$ ).

### 3.4. Detection of Surface and Precursor Species

Our wavelength-dependent analysis revealed that Raman spectroscopy can be employed for the detection of surface and/or precursor species in electrode materials. As we will discuss in the following section, UV Raman spectra, in particular, shows a high sensitivity towards surface species, such as  $\text{Li}_2\text{CO}_3$ . Figure 5 depicts the Raman spectra of  $\text{LiNiO}_2$  at  $257\text{ nm}$  excitation, in comparison to those of reference compounds. The spectrum of  $\text{LiNiO}_2$  is characterized by a broad Ni-related feature at around  $530\text{ cm}^{-1}$ , which exhibits a shoulder at around  $460\text{ cm}^{-1}$ , as well as additional features at  $276$ ,  $1065$  (shoulder),  $1089$  and  $1454\text{ cm}^{-1}$ . To the best of our knowledge, only the visible Raman spectra of  $\text{LiNiO}_2$  were reported, to date, showing more pronounced peaks at around  $540$  and  $470\text{ cm}^{-1}$ , attributed to the  $E_g$  and  $A_{1g}$  mode, respectively [12,32,40]. The additional signals we detected at  $276$ ,  $1089$  and  $1454\text{ cm}^{-1}$ , can readily be assigned by comparison with a  $\text{Li}_2\text{CO}_3$  reference (see Figure 5). In particular, the signals at  $1089$  and  $1454\text{ cm}^{-1}$  were attributed to symmetric and asymmetric carbonate stretching, respectively, whereas the small feature at  $276\text{ cm}^{-1}$  was not covered by calculations [41–43], and the small shoulder feature at around  $1065\text{ cm}^{-1}$  will be discussed below.

The presence of additional (non-oxidic) Raman features was also observed for the  $\text{LiNi}_x\text{Co}_{1-x}\text{O}_2$  mixed oxides. In fact, as can be seen in Figure 2D, at  $257\text{ nm}$  excitation, two signals are detected at  $1067$  and  $1093\text{ cm}^{-1}$ . Based on the above discussion, the signal at  $1093\text{ cm}^{-1}$  can be attributed to carbonate. Interestingly, with higher nickel content, the  $1093\text{ cm}^{-1}$  signal increases in intensity (see Figure 2D), suggesting an increased affinity of Ni-rich mixed oxides towards  $\text{Li}_2\text{CO}_3$  formation under ambient conditions. On the other hand, the position of the signal at  $1067\text{ cm}^{-1}$  is consistent with the symmetric stretching vibration of nitrate, as evidenced by a comparison with the spectrum of a  $\text{LiNO}_3$  reference (see Figure S6) [44]. The presence of nitrate may originate from precursors used for the synthesis, which were not completely decomposed during the calcination treatment. As discussed in the context of Figure 1, the Raman spectrum of  $\text{LiCoO}_2$  at  $257$  excitation shows a small signal at  $\sim 1070\text{ cm}^{-1}$ , which does not originate from resonance effects. In light of the above discussion, an assignment to nitrate stretching seems likely. On the other hand, the Raman spectrum of NMC (see Figure 4) shows no additional signal indicating the presence of nitrate. The different behavior may result from the different calcination temperatures for

$\text{LiNi}_x\text{Co}_{1-x}\text{O}_2$  and NMC. In fact,  $\text{LiNi}_x\text{Co}_{1-x}\text{O}_2$  was calcined at 775 °C (10 h) and NMC at 900 °C (15 h), strongly suggesting an incomplete decomposition of  $\text{LiNO}_3$  in the case of  $\text{LiNi}_x\text{Co}_{1-x}\text{O}_2$ . In this context, it should be mentioned that for  $\text{LiNi}_x\text{Co}_{1-x}\text{O}_2$  mixed oxides, a calcination temperature of 775 °C was chosen to minimize the cation disorder [45]. To summarize, the above studies show that deep UV excitation at 257 nm allows for the sensitive detection of surface species and/or precursor species reminiscent of the synthesis.

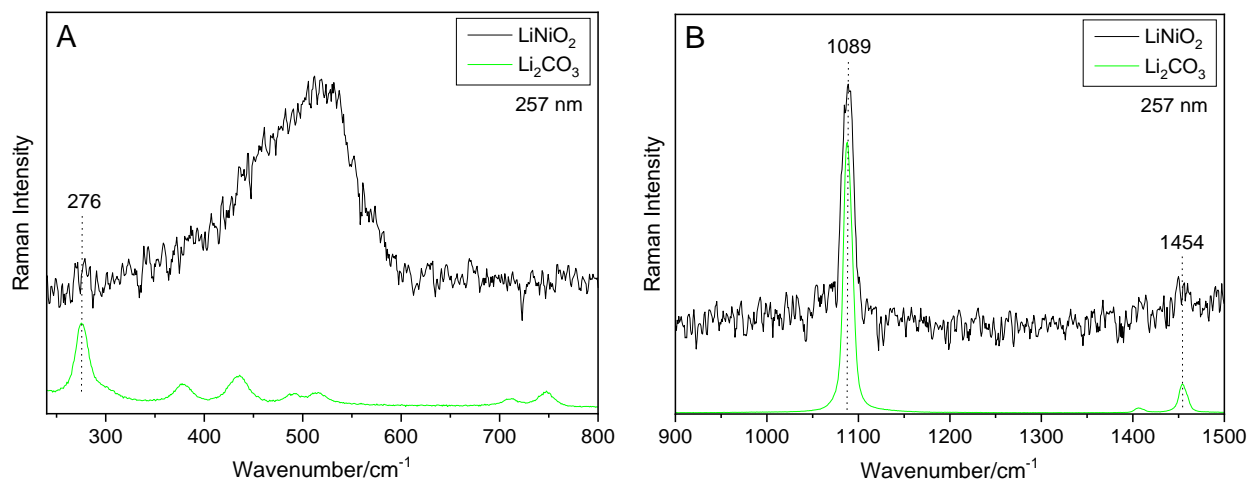


**Figure 5.** Raman spectra of  $\text{LiNiO}_2$  and  $\text{Li}_2\text{CO}_3$  (reference) at 257 nm excitation. (A) Low-wavenumber region. (B) Region within 900–1500  $\text{cm}^{-1}$ . Spectra were offset for clarity.

#### 4. Conclusions

The further development of lithium-ion batteries will strongly depend on a detailed understanding of the structure–stability–function relationships of the cathodes, which largely limit the energy density and dominate the battery cost. Raman spectroscopy was shown to be a powerful tool to enhance the structural insight into layered cathode materials also under electrochemical conditions.

For the further development of the technique towards cathode characterization, we systematically applied multi-wavelength Raman spectroscopy to common layered cathode materials ( $\text{LiCoO}_2$ ,  $\text{LiNi}_x\text{Co}_{1-x}\text{O}_2$ , NMC) for the first time. The variation of the laser excitation from the deep UV to the visible (257, 385, 515, 633 nm) allowed us gain new insight into the (electronic) structure, by analyzing the wavelength-dependent spectral profiles. For  $\text{LiCoO}_2$ , a resonance effect was observed, which was most pronounced for 385 nm excitation and lead to the appearance of overtone/combination bands, in addition to the intensity changes of the fundamental modes. In  $\text{LiNi}_x\text{Co}_{1-x}\text{O}_2$  mixed oxides and NMC, the overtone features persisted but were mitigated by the presence of Ni and/or Mn, highlighting the sensitivity of the resonance effect on electronic structure changes.

The use of UV excitation was demonstrated to further enhance the possibilities of the Raman technique in the context of cathode characterization. First, laser excitation in the near UV (385 nm) and deep UV (257 nm) was shown to increase the sensitivity towards Ni in NMC, as compared to the employed visible wavelengths (515, 633 nm). Moreover, using 257 nm laser excitation, we demonstrated that the nickel content in  $\text{LiNi}_x\text{Co}_{1-x}\text{O}_2$  (and NMC) materials can be quantified, which is of great interest also for other nickel containing layered materials. Future studies may be directed towards a quantitative analysis of spectral profiles by combining experiment with theoretical calculations. Secondly, deep UV excitation at 257 nm was shown to provide a sensitive detection of surface species and/or precursor species reminiscent of the synthesis. In particular, we identified carbonate and nitrate species by comparison with reference compounds. To this end, future work may specify the sensitivity for surface species/impurity detection by a comparison with dedicated surface and bulk analysis.

Our results demonstrate the potential of multi-wavelength Raman spectroscopy for the characterization of layered cathode materials for lithium-ion batteries, allowing for phase identification and quantification, insight into the electronic structure as well as surface species/impurity detection.

**Supplementary Materials:** The following supporting information can be downloaded at: <https://www.mdpi.com/article/10.3390/batteries8020010/s1>. Results from XRD diffraction, UV-Vis spectroscopy, UV Raman spectroscopy and visible Raman spectroscopy of layered oxide materials as well as reference compounds.

**Author Contributions:** Conceptualization, C.H.; Investigation, M.H. and K.H.; Data Analysis, M.H. and K.H.; Writing—Original Draft Preparation, M.H. and C.H.; Writing—Review and Editing, M.H., K.H. and C.H.; Supervision, Project Administration, Funding Acquisition, C.H. All authors have read and agreed to the published version of the manuscript.

**Funding:** This work was supported by the Deutsche Forschungsgemeinschaft (DFG, HE 4515/8-1).

**Institutional Review Board Statement:** Not applicable.

**Informed Consent Statement:** Not applicable.

**Data Availability Statement:** Not applicable.

**Acknowledgments:** The authors thank Philipp Waleska and Simone Rogg for performing the UV Raman measurements.

**Conflicts of Interest:** The authors declare no competing financial interest.

## References

1. Etacheri, V.; Marom, R.; Elazari, R.; Salitra, G.; Aurbach, D. Challenges in the development of advanced Li-ion batteries: A review. *Energy Environ. Sci.* **2011**, *4*, 3243–3262. [[CrossRef](#)]
2. Nitta, N.; Wu, F.; Lee, J.T.; Yushin, G. Li-ion battery materials: Present and future. *Mater. Today* **2015**, *18*, 252–264. [[CrossRef](#)]
3. Manthiram, A. A reflection on lithium-ion battery cathode chemistry. *Nat. Commun.* **2020**, *11*, 1550. [[CrossRef](#)] [[PubMed](#)]
4. Liu, H.S.; Zhang, Z.R.; Gong, Z.L.; Yang, Y. Origin of deterioration for LiNiO<sub>2</sub> cathode material during storage in air. *Electrochem. Solid-State Lett.* **2004**, *7*, A190–A193. [[CrossRef](#)]
5. Yabuuchi, N.; Ohzuku, T. Novel lithium insertion material of LiCo<sub>1/3</sub>Ni<sub>1/3</sub>Mn<sub>1/3</sub>O<sub>2</sub> for advanced lithium-ion batteries. *Power Sources* **2003**, *171*, 119–121. [[CrossRef](#)]
6. Liu, W.; Oh, P.; Liu, X.; Lee, M.J.; Cho, W.; Chae, S.; Kim, Y.; Cho, J. Nickel-rich layered lithium transition-metal oxide for high-energy lithium-ion batteries. *Angew. Chem. Int. Ed.* **2015**, *54*, 4440–4457. [[CrossRef](#)]
7. Guo, B.; Zhao, J.H.; Fan, X.M.; Zhang, W.; Li, S.; Yang, Z.H.; Chen, Z.X.; Zhang, W.X. Aluminum and fluorine co-doping for promotion of stability and safety of lithium-rich layered cathode material. *Electrochim. Acta* **2017**, *236*, 171–179. [[CrossRef](#)]
8. Hausbrand, R.; Cherkashinin, G.; Ehrenberg, H.; Gröting, M.; Albe, K.; Hess, C.; Jaegermann, W. Fundamental degradation mechanisms of layered oxide Li-ion battery cathode materials: Methodology, insights and novel approaches. *Mater. Sci. Eng. B.* **2015**, *192*, 3–25. [[CrossRef](#)]
9. Pender, J.P.; Jha, G.; Youn, D.H.; Ziegler, J.M.; Andoni, I.; Choi, E.J.; Heller, A.; Dunn, B.S.; Weiss, P.S.; Penner, R.M.; et al. Electrode degradation in lithium-ion batteries. *ACS Nano* **2020**, *14*, 1243–1295. [[CrossRef](#)]
10. Baddour-Hadjean, R.; Pereira-Ramos, J.P. Raman microspectrometry applied to the study of electrode materials for lithium batteries. *Chem. Rev.* **2010**, *110*, 1278–1319. [[CrossRef](#)]
11. Tripathi, A.M.; Su, W.N.; Hwang, B.J. *In situ* analytical techniques for battery interface analysis. *Chem. Soc. Rev.* **2018**, *47*, 736–851. [[CrossRef](#)] [[PubMed](#)]
12. Flores, E.; Novák, P.; Berg, E.J. *In situ* and *operando* Raman spectroscopy of layered transition metal oxides for Li-ion battery cathodes. *Front. Energy Res.* **2018**, *6*, 82. [[CrossRef](#)]
13. Julien, C.M.; Mauger, A. *In situ* Raman analyses of electrode materials for Li-ion batteries. *AIMS Mater. Sci.* **2018**, *5*, 650. [[CrossRef](#)]
14. Flores, E.; Novák, P.; Aschauer, U.; Berg, E.J. Cation Ordering and Redox Chemistry of Layered Ni-Rich Li<sub>x</sub>Ni<sub>1-2y</sub>Co<sub>y</sub>Mn<sub>y</sub>O<sub>2</sub>: An *Operando* Raman Spectroscopy Study. *Chem. Mater.* **2020**, *32*, 186–194. [[CrossRef](#)]
15. Jehnichen, P.; Korte, C. *Operando* Raman Spectroscopy Measurements of a High-Voltage Cathode Material for Lithium-Ion Batteries. *Anal. Chem.* **2019**, *91*, 8054–8061. [[CrossRef](#)]
16. Matsuda, Y.; Kuwata, N.; Okawa, T.; Dorai, A.; Kamishima, O.; Kawamura, J. *In situ* Raman spectroscopy of Li<sub>x</sub>CoO<sub>2</sub> cathode in Li/Li<sub>3</sub>PO<sub>4</sub>/LiCoO<sub>2</sub> all-solid-state thin-film lithium battery. *Solid State Ionics* **2019**, *335*, 7–14. [[CrossRef](#)]
17. Otoyama, M.; Ito, Y.; Sakuda, A.; Tatsumisago, M.; Hayashi, A. Reaction uniformity visualized by Raman imaging in the composite electrode layers of all-solid-state lithium batteries. *Phys. Chem. Chem. Phys.* **2020**, *22*, 13271–13276. [[CrossRef](#)]

18. Flores, E.; Mozhzhukhina, N.; Aschauer, U.; Berg, E.J. *Operando* Monitoring the Insulator–Metal Transition of LiCoO<sub>2</sub>. *ACS Appl. Mater. Interfaces* **2021**, *13*, 22540–22548. [[CrossRef](#)]
19. Yellampalle, B.; Sluch, M.; Asher, S.; Lemoff, B. Multiple-excitation-wavelength resonance-Raman explosives detection. *Proc. SPIE* **2011**, *8018*, 801819.
20. Gross, T.; Hess, C. Raman diagnostics of LiCoO<sub>2</sub> electrodes for lithium-ion batteries. *J. Power Sources* **2014**, *256*, 220–225. [[CrossRef](#)]
21. Julien, C.M.; Massot, M.; Ramana, C.V. Structure of electrode materials for Li-ion batteries: The Raman spectroscopy investigations. In *Portable and Emergency Energy Sources*; Stoynov, Z., Vladikova, D., Eds.; Martin Drinov Academic Publishing House: Sofia, Bulgaria, 2006.
22. Ammundsen, B.; Burns, G.R.; Islam, M.S.; Kanoh, H.; Rozière, J. Lattice dynamics and vibrational spectra of lithium manganese oxides: A computer simulation and spectroscopic study. *J. Phys. Chem. B* **1999**, *103*, 5175–5180. [[CrossRef](#)]
23. Lei, J.; McLarnon, F.; Kostecki, R. In situ raman microscopy of individual LiNi<sub>0.8</sub>Co<sub>0.15</sub>Al<sub>0.05</sub>O<sub>2</sub> particles in a Li-ion battery composite cathode. *J. Phys. Chem. B* **2005**, *109*, 952–957. [[CrossRef](#)] [[PubMed](#)]
24. Dokko, K.; Mohamedi, M.; Anzue, N.; Itoh, T.; Uchida, I. In situ Raman spectroscopic studies of LiNi<sub>x</sub>Mn<sub>2-x</sub>O<sub>4</sub> thin film cathode materials for lithium ion secondary batteries. *J. Mater. Chem.* **2002**, *12*, 3688–3693. [[CrossRef](#)]
25. Kerlau, M.; Marcinek, M.; Srinivasan, V.; Kostecki, R.M. Studies of local degradation phenomena in composite cathodes for lithium-ion batteries. *Electrochim. Acta* **2007**, *53*, 1385–1392. [[CrossRef](#)]
26. Pechini, P.M. Method of Preparing Lead and Alkaline Earth Titanates and Niobates and Coating Method Using the Same to form a Capacitor. U.S. Patent Nr. 3.330.697, 11 July 1967.
27. Toby, B.H.; Von Dreele, R.B. GSAS-II: The genesis of a modern open-source all purpose crystallography software package. *J. Appl. Cryst.* **2013**, *46*, 544–549. [[CrossRef](#)]
28. Inaba, M.; Iriyama, Y.; Ogumi, Z.; Todzuka, Y.; Tasaka, A. Raman study of layered rock-salt LiCoO<sub>2</sub> and its electrochemical lithium deintercalation. *J. Raman Spectrosc.* **1997**, *28*, 613–617. [[CrossRef](#)]
29. Ghosh, P.; Mahanty, S.; Raja, M.W.; Basu, R.N.; Maiti, H.S. Structure and optical absorption of combustion-synthesized nanocrystalline LiCoO<sub>2</sub>. *J. Mater. Res.* **2006**, *22*, 1162–1167. [[CrossRef](#)]
30. Rao, K.J.; Benqlilou-Moudden, H.; Desbat, B.; Vinatier, P.; Levasseur, A. Infrared spectroscopic study of LiCoO<sub>2</sub> thin films. *J. Solid State Chem.* **2002**, *165*, 42–47. [[CrossRef](#)]
31. Julien, C. Local cationic environment in lithium nickel–cobalt oxides used as cathode materials for lithium batteries. *Solid State Ionics* **2000**, *136–137*, 887–896. [[CrossRef](#)]
32. Inaba, M.; Todzuka, Y.; Yoshida, H.; Grincourt, Y.; Tasaka, A.; Tomida, Y.; Ogumi, Z. Raman spectra of LiCo<sub>1-y</sub>Ni<sub>y</sub>O<sub>2</sub>. *Chem. Lett.* **1995**, *24*, 889–890. [[CrossRef](#)]
33. Kalyani, P.; Kalaiselvi, N. Various aspects of LiNiO<sub>2</sub> chemistry: A review. *Sci. Technol. Adv. Mater.* **2005**, *6*, 689–703. [[CrossRef](#)]
34. Chakraborty, A.; Dixit, M.; Aurbach, D.; Major, D.T. Predicting accurate cathode properties of layered oxide materials using the SCAN meta-GGA density functional. *NPJ Comput. Mater.* **2018**, *4*, 60. [[CrossRef](#)]
35. Laubach, S.; Laubach, S.; Schmidt, P.C.; Ensling, D.; Schmid, S.; Jaegermann, W.; Thißen, A.; Nikolowski, K.; Ehrenberg, H. Changes in the crystal and electronic structure of LiCoO<sub>2</sub> and LiNiO<sub>2</sub> upon Li intercalation and de-intercalation. *Phys. Chem. Chem. Phys.* **2009**, *11*, 3278–3289. [[CrossRef](#)] [[PubMed](#)]
36. Dahn, J.R.; von Sacken, U.; Michal, C.A. Structure and electrochemistry of Li<sub>1±y</sub>NiO<sub>2</sub> and a new Li<sub>2</sub>NiO<sub>2</sub> phase with the Ni(OH)<sub>2</sub> structure. *Solid State Ionics* **1990**, *44*, 87–97. [[CrossRef](#)]
37. Zhang, X.; Mauger, A.; Lu, Q.; Groult, H.; Perrigaud, L.; Gendron, F.; Julien, C.M. Synthesis and characterization of LiNi<sub>1/3</sub>Mn<sub>1/3</sub>Co<sub>1/3</sub>O<sub>2</sub> by wet-chemical method. *Electrochim. Acta* **2010**, *55*, 6440–6449. [[CrossRef](#)]
38. Ruther, R.E.; Callender, A.F.; Zhou, H.; Martha, S.K.; Nanda, J. Raman microscopy of lithium-manganese-rich transition metal oxide cathodes. *Electrochem. Soc.* **2015**, *162*, A98. [[CrossRef](#)]
39. Ghanty, C.; Markovsky, B.; Erickson, E.M.; Talianker, M.; Haik, O.; Tal-Yossef, Y.; Mor, A.; Aurbach, D.; Lampert, J.; Volkov, A.; et al. Li<sup>+</sup>-ion extraction/insertion of Ni-rich Li<sub>1+x</sub>(Ni<sub>y</sub>Co<sub>z</sub>Mn<sub>z</sub>)<sub>w</sub>O<sub>2</sub> (0.005 < x < 0.03; y:z = 8:1, w ≈ 1) electrodes: In situ XRD and Raman spectroscopy study. *ChemElectroChem* **2015**, *2*, 1479–1486.
40. Julien, C.M.; Massot, M. Raman scattering of LiNi<sub>1-y</sub>Al<sub>y</sub>O<sub>2</sub>. *Solid State Ionics* **2002**, *148*, 53–59. [[CrossRef](#)]
41. Brooker, M.H.; Bates, J.B. Raman and infrared spectral studies of anhydrous Li<sub>2</sub>CO<sub>3</sub> and Na<sub>2</sub>CO<sub>3</sub>. *J. Chem. Phys.* **1971**, *54*, 4788–4796. [[CrossRef](#)]
42. Koura, N.; Kohara, S.; Takeuchi, K.; Takahashi, S.; Curtiss, L.A. Alkali carbonates: Raman spectroscopy, ab initio calculations, and structure. *J. Mol. Struct.* **1996**, *382*, 163–169. [[CrossRef](#)]
43. Brooker, M.H.; Wang, J. Raman and infrared studies of lithium and cesium carbonates. *Spectrochim. Acta* **1992**, *48A*, 999–1008. [[CrossRef](#)]
44. James, D.W.; Leong, W.H. Structure of molten nitrates. III. Vibrational spectra of LiNO<sub>3</sub>, NaNO<sub>3</sub>, and AgNO<sub>3</sub>. *J. Chem. Phys.* **1969**, *51*, 640–646. [[CrossRef](#)]
45. Gross, T.; Buhmester, T.; Bramnik, K.G.; Bramnik, N.N.; Nikolowski, K.; Baetz, C.; Ehrenberg, H.; Fuess, H. Structure–intercalation relationships in LiNi<sub>y</sub>Co<sub>1-y</sub>O<sub>2</sub>. *Solid State Ionics* **2005**, *176*, 1193–1199. [[CrossRef](#)]